mater.scichina.com link.springer.com

Published online 8 July 2022 | https://doi.org/10.1007/s40843-022-2092-0
Sci China Mater 2022, 65(11): 2997–3006

Electronic modulation and structure engineered $MoSe_2$ with multichannel paths as an advanced anode for sodium-ion half/full batteries

Chengkui Lv[1,2†], Chunfa Lin[2†], Huilong Dong[2†], Huaixin Wei[1*], Jun Yang[3*] and Hongbo Geng[2*]

ABSTRACT **Owing to the abundance and low price of sodium, researches on sodium-ion batteries (SIBs) as a lithium-ion battery (LIB) alternative are emerging as a consensus. It is crucial to develop electrode materials suitable for sodium storage. In recent years, two-dimensional (2D) layered transition metal disulfide compounds (TMDs) have trigered interest in the realm of energy and environmental fields. In particular, $MoSe_2$ is thought to be a suitable material for SIBs due to its wide original layer spacing and high conductivity. Herein, N-doped dual carbon-coated $MoSe_2$ with multichannel paths ($MoSe_2$/multichannel carbon nanofibers (MCFs)@NC) is fabricated *via* electrospinning, followed by a selenation and carbonization process. The existence of a 3D conductive network, abundant void spaces, and sufficient electron transportation pathways are conducive to rapid and fast charge transfer kinetics under volume expansion stress. When applied in SIBs, the $MoSe_2$/MCFs@NC shows a high capability (319 mA h g^{-1} at 10 A g^{-1}), as well as good cycling stability (303 mA h g^{-1} after 1100 cycles at 10 A g^{-1}). Furthermore, coupled with the $Na_3V_2(PO_4)_2O_2F$ cathode, the full cell also exhibits excellent performance. The theoretical calculation of the $MoSe_2$/MCFs@NC confirms that the superiority of its SIB performance is owing to the strong interaction between the double-doped carbon and $MoSe_2$. This scheme provides a wide space for preparing high-performance electrode materials for SIBs.**

Keywords: dual carbon-coated, multichannel paths, sodium-ion batteries, full batteries, theoretical calculation

INTRODUCTION

Due to the increasing energy crisis, clean energy has attracted extensive attention [1,2]. In recent years, lithium-ion batteries (LIBs) have been commonly used in mobile electronic devices and electric vehicles as efficient energy storage devices [3–5]. However, Due to the lack of lithium resources, LIBs will not meet the market demand in the long term [6–8]. Due to the low cost and abundant storage of sodium, sodium-ion batteries (SIBs), which have a similar energy storage mechanism with LIBs, have been regarded as a promising candidate [9–11]. Even though lithium and sodium belong to the same group and have similar physicochemical characteristics, the large sodium ion radius shows slow diffusion dynamics during the Na^+ (de)sodiation in the electrode materials, resulting in sluggish kinetics and large structural changes of the active materials during the cycling [12–14]. Because conventional graphite structures cannot be directly applied to SIBs, designing and developing suitable anodes for practical application in SIBs are desired.

Transition metal disulfides (TMDs) have gained great attention in the field of power supply and conversion devices [15–19]. TMDs are more stable with a unique defect structure due to the existence of lone pair d electrons and empty d orbitals that are easy to bond, as well as the high charge/radius ratio of atoms or ions. Among them, $MoSe_2$ possesses several appealing features, including a large interlayer distance (~0.64 nm), a high theoretical capacity (422 mA h g^{-1}), and a small bandgap (~1.5 eV) [20–22]. The van der Waals (vdW) forces between Mo–Se bonds are comparable to those between Mo–O or Mo–S bonds, favoring kinetic conversion reactions for SIBs [23]. However, the poor cycling stability of $MoSe_2$ derived from the structural collapse during the repeated extraction and insertion of sodium ions is a mountain ahead of its application in SIBs. Improving the sodium storage performance of $MoSe_2$ by rational design is an effective way to enhance the performance of SIBs. The hybridization of $MoSe_2$ and carbon-based materials can improve the overall performance of SIBs. Liu *et al.* [24] designed an encapsulation-type structured $MoSe_2$@hollow carbon nanosphere material, which showed a high capacity of 471 mA h g^{-1} over 1000 cycles at 3 A g^{-1}. Wu *et al.* [25] produced $MoSe_2$@NPC/rGO composites with a few layers of $MoSe_2$ encased by N/P co-doped carbon and reduced grapheme oxide (rGO), which had a high specific capacity of 100 mA h g^{-1} even at 50 A g^{-1}. Ultrathin two-dimensional (2D) $MoSe_2$ nanosheets can grow on 3D ordered macroporous carbon by a simple hydrothermal reaction, displaying an outstanding rate capability (279 mA h g^{-1} at 10 A g^{-1}) [26]. Although a composite of $MoSe_2$ and conductive carbon material can improve the conductivity, it cannot buffer more than 300% of its volume change during the cycle [27–29]. Therefore, it often shows a low-rate performance when used as the anode of SIBs. It is particularly important to build continuous and connected multichannel with plentiful voids to adapt to its stress relief through simple design methods. In parallel, the electronic transportation capacity of $MoSe_2$ is improved to further enhance the comprehensive performance of

[1] School of Chemistry and Life Sciences, Suzhou University of Science and Technology, Suzhou 215009, China
[2] School of Materials Engineering, Changshu Institute of Technology, Changshu 215500, China
[3] School of Material Science & Engineering, Jiangsu University of Science and Technology, Zhenjiang 212003, China
† These authors contributed equally to this work.
* Corresponding authors (emails: hxwei@usts.edu.cn (Wei H); hbgeng@cslg.edu.cn (Geng H); iamjyang@just.edu.cn (Yang J))

SIBs. The multistage distribution also could inhibit the aggregation of active substances and make the electrode material in full contact with the electrolyte.

Herein, a designable structure of N-doped dual carbon-modified $MoSe_2$ is reported. Multichannel carbon nanofibers (MCFs) were prepared *via* electrospinning followed by subsequent coupling with $MoSe_2$ and carbonization ($MoSe_2$/MCFs@NC). As nanofillers, the MCFs and carbon coating can inhibit the $MoSe_2$ re-stacking, enabling the formation of homogeneous $MoSe_2$ nanosheets with an extended (002) crystal plane layer spacing structure (0.68 nm). In addition, the $MoSe_2$/MCFs@NC has many structural features that are favorable for sodium-ion (de)embedding: (1) $MoSe_2$ loading on MCFs and carbon coating improve the charge transfer kinetics and reduce the charge transfer resistance; (2) increased $MoSe_2$ layer spacing promotes the diffusion of sodium ions; (3) the N-doped carbon nanosheets strengthen the contact of active substances during the cycling process and buffer the volume expansion of $MoSe_2$. The $MoSe_2$/MCFs@NC anode for SIBs has an outstanding rate performance of 319 mA h g^{-1} at 10 A g^{-1} and good cycling performance (303 mA h g^{-1} at 10 A g^{-1} after 1100 cycles). An energy density of 104 W h kg^{-1} can also be achieved in the full batteries at a power density of 226 W kg^{-1}, showing the practical application of $MoSe_2$/MCFs@NC in SIBs. The good SIB performance of the $MoSe_2$/MCFs@NC electrode is verified by theoretical simulation and reaction kinetics analysis.

EXPERIMENTAL SECTION

Synthesis of MCFs

Polyacrylonitrile (PAN, 0.4 g) and polystyrene (PS, 0.4 g) were dissolved in 5 mL of *N*,*N*-dimethylformamide at 60°C for 12 h with magnetic stirring in an oil bath to obtain a homogeneous pale yellow precursor solution. Then, the above solution was transferred to a 5-mL syringe for electrospinning. The working voltage and flow rate of electrospinning were adjusted to 12 kV and 0.8 mL h^{-1}, respectively. Next, the prepared spinning samples were separated from the aluminum foil, and stabilized in an air atmosphere at 260°C for 2 h, followed by the carbonization of the pre-oxidized carbon fibers at 900°C in a nitrogen atmosphere for 2 h to obtain MCFs.

Synthesis of $MoSe_2$/MCFs

The selenium powder (1 mmol) was dissolved in 5 mL of $N_2H_4{\cdot}H_2O$ (85%) solution for 1 h with stirring. Meanwhile, $Na_2MoO_4{\cdot}2H_2O$ (0.5 mmol) was dissolved in deionized water (20 mL). The previously prepared MCFs (40 mg) were put into the Na_2MoO_4 solution, and then ultrasonically treated for 1 h to achieve a homogenous mixture. The reduced selenium solution was then added to the aforesaid combination, sealed, and heated to 200°C for 12 h with the hydrothermal method. The product was cleaned thrice with deionized water/ethanol and dried at 60°C in a vacuum. Finally, the product was heated to 500°C for 2 h under H_2 (5 vol%)/Ar (95 vol%) (denoted as $MoSe_2$/MCFs). In comparison, pure $MoSe_2$ was prepared with the similar method but without the addition of MCFs.

Synthesis of $MoSe_2$/MCFs@NC

In 100 mL of tris-buffer solution, 40 mg of $MoSe_2$/MCFs were dispersed (10 mmol L^{-1}). Then, for the next 6 h, 40 mg of dopamine hydrochloride was added with magnetic stirring. The product was centrifuged and washed with deionized water and ethanol thrice. Then the as-prepared $MoSe_2$/MCFs@polydopamine (PDA) was treaded by heating at 500°C for 3 h in N_2 after being dried at 60°C in a vacuum to get $MoSe_2$/MCFs@NC.

Characterization

The as-prepared $MoSe_2$/MCFs@NC was characterized by scanning electron microscopy (SEM, Hitachi SU-9010), X-ray diffractometer (XRD, D/MAX-2000), transition electron microscope (TEM, Tecani G-20), and X-ray photoelectron spectrometer (XPS, Thermo Scientific, ESCALAB 250Xi).

Electrochemical measurements

To test the electrochemical characteristics, the composite $MoSe_2$/MCFs@NC was constructed into a half-cell. The electrodes were made up of active materials, carbon nanotubes (CNT), and polyvinylidene fluoride (7:2:1 weight ratio) in *N*-methyl pyrrolidone. The slurry was applied evenly on the copper foil with an active material mass loading of 1–1.5 mg cm^{-2} and then was vacuum dried (60°C, 12 h). The electrolyte and separator were 1.0 mol L^{-1} $NaPF_6$ in 1,2-dimethoxyethane and a glass fiber film, respectively. Extensive electrochemical testing experiments were conducted on the battery test system and workstation, such as galvanostatic charge/discharge (GCD), electrochemical impedance spectrum (EIS, 10^{-2} to 10^{-5} Hz), and cyclic voltammetry (CV) curves (0.01–3.00 V). The mass ratio of the anode and cathode was 1:6. Before assembling a full cell, the $MoSe_2$/MCFs@NC anode was presodiated in a half-cell for five cycles at 0.1 A g^{-1} (0.01–3 V). The electrolyte and separator were the same as those of half cells. The calculation of energy density for the full cells was based on the total mass of the anode and cathode electrodes, as well as the median voltage of the batteries.

Computational methods

Density functional theory (DFT) calculations were performed to obtain the adsorption and diffusion performance of sodium ions. Within the framework of generalized gradient approximation, the study of electronic exchange and correlation effects was based on the Perdew-Burke-Ernzerhof functional (GGA-PBE) and the double numerical atomic orbital with polarized p-function (DNP) [30]. Grimme's dispersion correction (DFT-D2) [31] was included to account for the vdW interactions. During geometry optimization, the threshold values were established at 1×10^{-5} Ha for convergence of energies, 1×10^{-3} Ha $Å^{-1}$ for gradient, and 5×10^{-3} Å for displacement. The $13 \times 13 \times 1$ and $17 \times 17 \times 1$ *k*-point meshes of 2H-$MoSe_2$ and carbon unit cells, respectively, were used for lattice optimization. The carbon nanofibers/$MoSe_2$ heterostructure ($MoSe_2$/MCFs) was modeled with the carbon 4×4 and $MoSe_2$ 3×3 supercell. And one of the carbon atoms was replaced by a nitrogen atom to obtain the nitrogen-doped $MoSe_2$/MCFs heterostructure ($MoSe_2$/MCFs@NC). It should be pointed out that the position of the doped N in carbon has a negligible influence on the total energy of $MoSe_2$/MCFs@NC according to our results. The bilayer $MoSe_2$ (BL-$MoSe_2$) with 3×3 supercells was used. The $4 \times 4 \times 1$ *k*-point mesh was used during the calculations of the BL-$MoSe_2$ 3×3 supercell and the heterostructures. The adsorption energy (E_{ads}) for a single Na atom was defined as:

$$E_{ads} = E_* + E_{Na} - E_{Na*},$$

where E_* is the adsorbent's energy and E_{Na} is the energy per atom in bulk Na. The total energy of the optimized adsorption

system is E_{Na^*}. The diffusion barriers (E_b) of the inserted Na in different inter surfaces were determined *via* transition state searches employing the full linear synchronous transit/quadratic synchronous transit (LST/QST) technique [32].

RESULTS AND DISCUSSION

Materials manufacturing

The overall fabrication sequence of $MoSe_2$/MCFs@NC composites is presented in Fig. 1a. Firstly, MCFs are prepared using PAN *via* thermal annealing treatment. During the process, PS acts as the pore-forming agent, and produces parallel channels within the carbonized PAN shells. Subsequently, MCFs and sheet-like $MoSe_2$ are compounded together by a hydrothermal reaction. The polydopamine is applied to obtain $MoSe_2$/MCFs@NC. The unique N-doped multichannel structure and external conductive carbon shell not only facilitate the internal channels for ion transport, but also accelerate electron transfer, favoring the electrochemical performance. The XRD characterizations of $MoSe_2$, $MoSe_2$/MCFs, and $MoSe_2$/MCFs@NC were conducted (Fig. 1b, and Figs S1a, S2a). Except for the broad peak around 21° attributed to amorphous carbon, other four diffraction peaks match well with the hexagonal phase of $MoSe_2$ (JCPDS No. 29-0914) accompanied by the space group of *P*63/*mmc*, confirming the absence of impure phases in the samples. With the introduction of conductive carbon, the peak intensity of carbon increases. It is worth noting that the (002) plane is slightly shifted to a lower angle due to the weak vdW interaction between layers of Se–Mo–Se, which is regulated by the annealing slope rate and structure, leading to expansion [33,34]. The Raman spectra of the samples (Fig. 1c) reveal that except for pure $MoSe_2$, the D band (1336 cm^{-1}) and G band (1595 cm^{-1}) correspond to the disordered carbon and graphitic carbon, respectively [35]. The intensity ratio of I_D/I_G of $MoSe_2$/MCFs@NC (1.12) is higher than that of MCFs (1.04), suggesting that the presence of more defects induced by doping with N [36], which is favorable for improving the electrical conductivity. XPS was detected to understand more details about the chemical components and valence states of $MoSe_2$/MCFs@NC. The survey spectrum (Fig. S3) reveals C, N, Mo, and Se elements in $MoSe_2$/MCFs@NC, where trace amount of oxygen is from the exposure to air. Fig. 1d displays the high-resolution C 1s spectrum. The peaks at 284.7, 285.8, and 288.6 eV are associated with C=C, C–C/C–N, and O–C=O, respectively [20]. An enhancement of the electronic coupling at the interface between $MoSe_2$ and MCFs is evidenced by the formation of the C–Mo bond (282.9 eV), accelerating electron transfer for the sodium storage [37]. Mo $3d_{5/2}$ (228.7 eV) and Mo $3d_{3/2}$ (231.8 eV) are in the Mo 3d XPS spectrum (Fig. 1e) [38]. In addition, a weak peak at 230.1 eV is indexed to Se 3s [39]. The Se 3d spectrum in Fig. 1f can be divided into Se $3d_{5/2}$ (54.3 eV) and Se $3d_{3/2}$ (55.2 eV). The wide peak of the intermediate belongs to the oxidation state of selenium [40]. Three peaks at 398.3, 399.7, and 401.2 eV in the N 1s XPS spectrum (Fig. 1g) can be ascribed to pyridinic-N, pyrrolic-N, and graphitic-N, respectively, creating abundant extrinsic

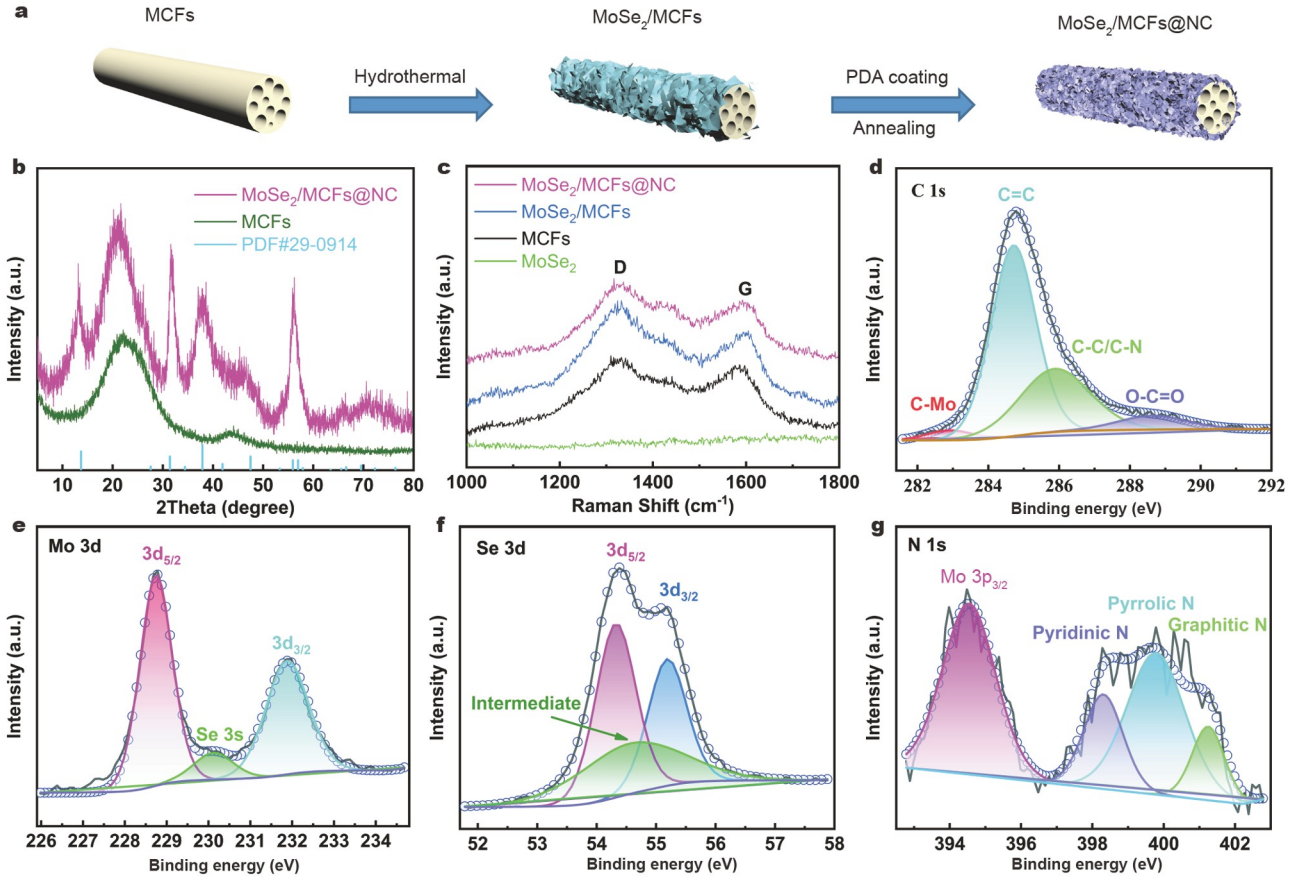

Figure 1 (a) Schematic of the preparation of $MoSe_2$/MCFs@NC. (b) XRD patterns of $MoSe_2$/MCFs@NC and MCFs. (c) Raman spectra for $MoSe_2$/MCFs@NC, $MoSe_2$/MCFs, MCFs, and $MoSe_2$. High-resolution XPS spectra of (d) C 1s, (e) Mo 3d, (f) Se 3d, and (g) N 1s for $MoSe_2$/MCFs@NC.

defects and active sites [41]. The large peak at 394.5 eV is the Mo $3p_{3/2}$ originated from Mo–N bonding [42].

The morphologies of MCF precursor and $MoSe_2$/MCFs were characterized *via* SEM and TEM. With an average diameter of ~500 nm, MCFs are well distributed as a connected network structure (Fig. 2a, b and Fig. S4a, b). The hollow structures in cross-sections can be confirmed by TEM (Fig. 2c and Fig. S4c, d). In addition, the SEM and TEM images of the pure sheet structure of $MoSe_2$ (Fig. S1b–d) show that the $MoSe_2$ nanosheets have successfully adhered to the surface of the MCFs without excessive aggregation (Fig. 2d, e, and Fig. S2b). The corresponding TEM images (Fig. 2f and Fig. S2c, d) also demonstrate the presence of internal pore channels. The element distribution of Mo, Se, and C is shown in the high-angle annular dark field (HAADF) and energy dispersive X-ray spectroscopy (EDX) mapping images (Fig. 2g). As depicted in Fig. 3a, the morphology of the $MoSe_2$/MCFs@NC composites is similar to that of the precursor $MoSe_2$/MCFs after coating by a carbon layer. In the magnified view of the composites (Fig. 3b), the sheet-like $MoSe_2$ becomes thicker due to complete encapsulation by the carbon layer. The internal pore structure allows the electrode to be exposed to more electrolytes, which provides a continuous electron transfer channel for the electrode and alleviates the volume change during charging and discharging. Fig. 3c, d demonstrate the carbon coating on the surface of $MoSe_2$ derived by PDA. The interface between $MoSe_2$ and the carbon layer can be clearly distinguished in Fig. 3e. In addition, the visible lattice fringes with an interplanar spacing of 0.68 nm are compatible with the $MoSe_2$ (002) crystal plane (Fig. 3f). This expanded layer spacing increases the storage capacity of sodium ions in the $MoSe_2$/MCFs@NC composites [24]. The HAADF and elemental mapping images of $MoSe_2$/MCFs@NC indicate the even distribution of C, N, Mo, and Se elements (Fig. 3g).

Electrochemical performance

The sodium storage performance of $MoSe_2$/MCFs@NC was systematically evaluated. The first five curves of the CV profiles of $MoSe_2$/MCFs@NC were obtained at 0.1 mV s^{-1}, as depicted in Fig. 4a. In the first cathodic sweep (discharge process), two major strong peaks at around 0.76 and 0.57 V are observed. The intercalation of Na^+ into $MoSe_2$ layers to generate Na_xMoSe_2 is the first reduction peak at 0.76 V, while another peak at 0.57 V corresponds to the further reduction of Na_xMoSe_2 to metallic Mo and Na_2Se, as well as the formation of the solid electrolyte interface (SEI) film [21,25]. The strong peak located near 0 V is caused by the Na^+ embedded in the multichannel carbon fiber

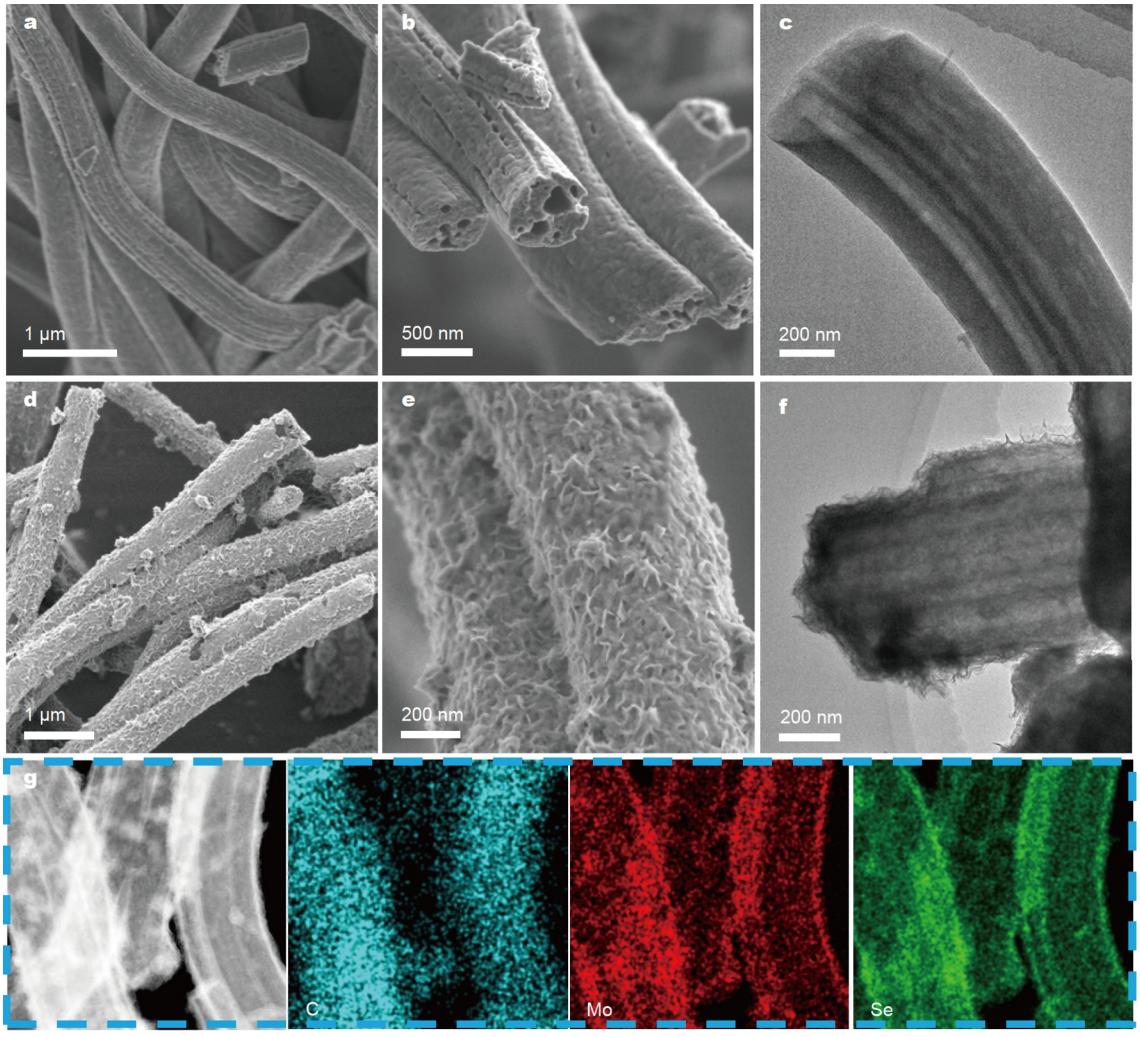

Figure 2 The morphology of MCFs and $MoSe_2$/MCFs. (a, b) SEM images and (c) TEM image of MCFs. (d, e) SEM images, (f) TEM image and (g) elemental mapping images of $MoSe_2$/MCFs.

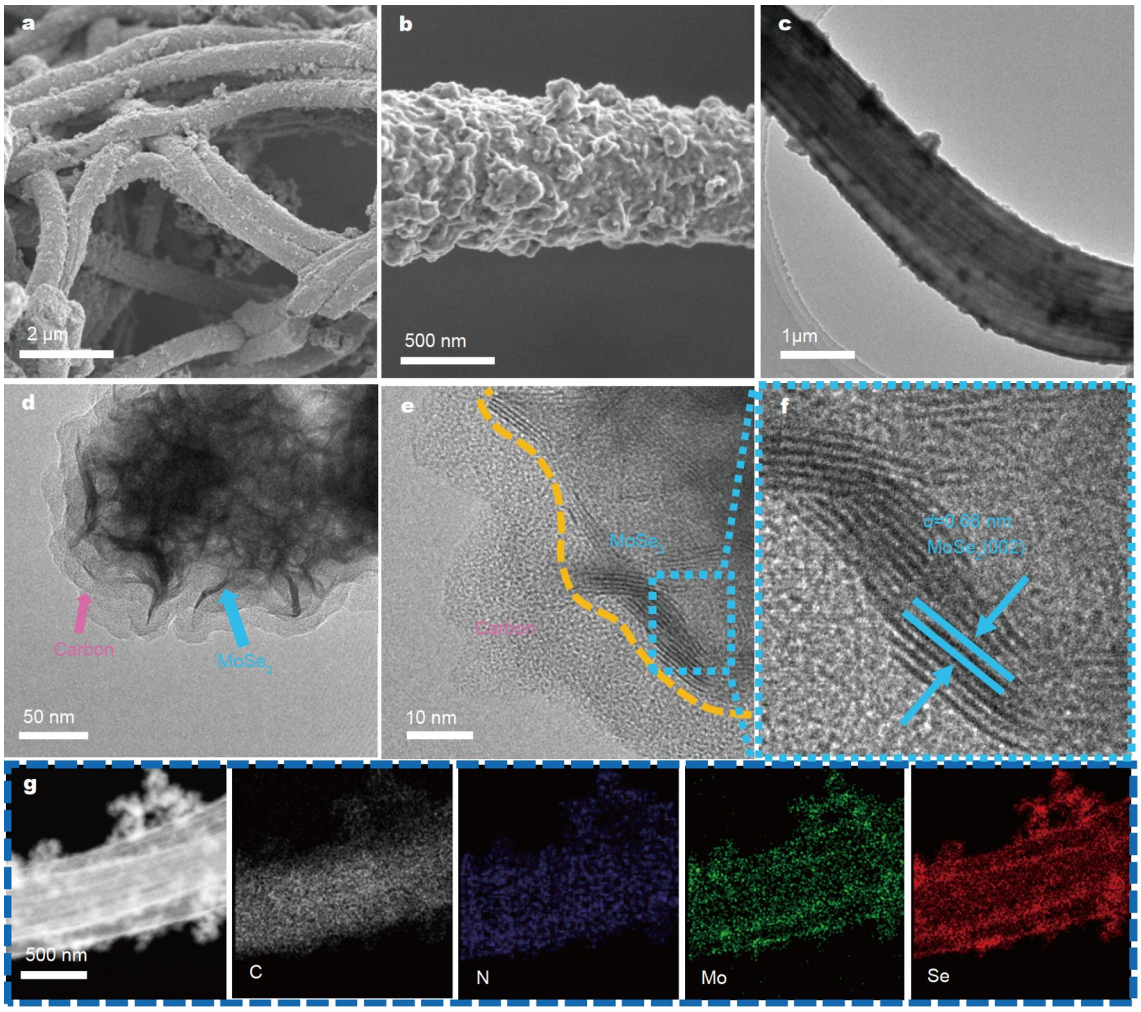

Figure 3 Morphology of $MoSe_2$/MCFs@NC. (a, b) SEM images. (c, d) TEM images. (e, f) HRTEM images. (g) Elemental mapping images.

[43–45]. In the subsequent anodic sweep (charge process), the reversed conversion reaction of Mo to $MoSe_2$ is responsible for the oxidation peak at 1.66 V [46]. In the next cycles, the almost overlapping cathode and anode curves suggest good electrochemical reversibility of $MoSe_2$/MCFs@NC. The GCD was performed to understand the storage capacity of the $MoSe_2$/MCFs@NC electrode at a current rate of 1 A g^{-1}. The discharge and charge plateaus, as illustrated in Fig. 4b, are compliant with the CV profile results. Furthermore, the $MoSe_2$/MCFs@NC anode has a first discharge specific capacity of 676 mA h g^{-1} and an initial Coulombic efficiency (CE) of 67.1%. The formation of SEI film and irreversible reactions are attributed to the capacity deterioration of the initial charge process, which is a common phenomenon. When $MoSe_2$/MCFs@NC was cycled at 1 A g^{-1}, a reversible capacity of 399 mA h g^{-1} was maintained after 100 cycles (Fig. 4c). The gradually increasing capacity of $MoSe_2$/MCFs@NC is a consequence of the phase transition of $MoSe_2$ from a highly crystalline to an amorphous state, which causes the active material to expand and store more ions. In particular, the outstanding sodium storage performance of the $MoSe_2$/MCFs@NC anodes was further confirmed by the rate test (Fig. 4d, e). The charge capacity below 1.0 V is calculated to be 150 mA h g^{-1} at 0.2 A g^{-1}, which is an extremely important parameter in practical use. The reversible capacities of $MoSe_2$/MCFs@NC are 411, 387, 374, 363, 344, and 319 mA h g^{-1} at 0.2, 0.5, 1.0, 2.0, 5.0, and 10.0 A g^{-1}, respectively, which are much higher than those obtained for $MoSe_2$/MCFs and pure $MoSe_2$ (Fig. S5). The discharge capacity can be restored to 409 mA h g^{-1} as the current rate is back to 0.2 A g^{-1}, revealing its favorable reversibility. While the rate performance of $MoSe_2$/MCFs and $MoSe_2$ electrodes is unsatisfactory, this further indicates that rational design with a multichannel carbon layer can significantly improve the electrochemical performance. This excellent rate performance is superior to other reported $MoSe_2$-based composites (Fig. 4f) [20,21,25,47–52]. The long-term longevity of $MoSe_2$/MCFs@NC at 10 A g^{-1} is depicted in Fig. 4g and Fig. S6. It is capable of achieving a discharge capacity of 303 mA h g^{-1} even after 1100 cycles. The excellent electrochemical performance of $MoSe_2$/MCFs@NC is due to the following: (1) the microporous multichannel structure not only increases the speed of the electron and ion transport, but also enhances the contact between the electrode and electrolyte, providing huge space for effective buffering of volume changes during the cycle; (2) $MoSe_2$ nanosheets are deposited on MCFs, providing more active sites for Na^+ insertion/extraction and shortening the ion diffusion path. As displayed in Fig. S7, the overall skeleton of the electrode is still visible after 20 cycles at 0.5 A g^{-1}, indicating that $MoSe_2$/MCFs@NC has excellent

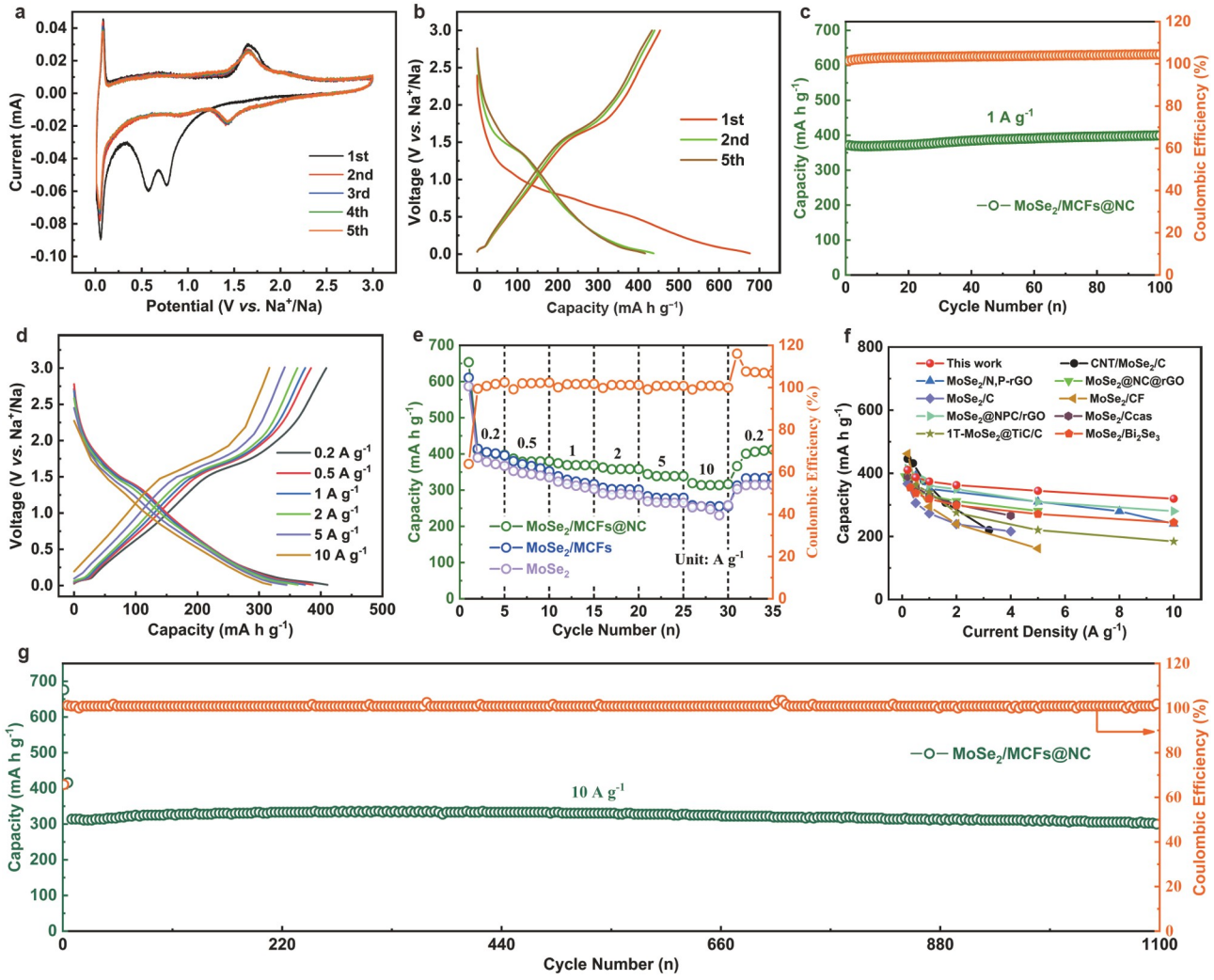

Figure 4 Electrochemical performance of the $MoSe_2$/MCFs@NC electrode. (a) CV curves at 0.1 mV s^{-1}. (b) Charge/discharge voltage profiles and (c) cycle performance at 1 A g^{-1}. (d) Charge/discharge curves at 0.2 to 10 A g^{-1}. (e) Rate performance of $MoSe_2$/MCFs@NC, $MoSe_2$/MCFs and $MoSe_2$. (f) Comparison of the rate capacity of the $MoSe_2$/MCFs@NC electrode with reported anodes based on $MoSe_2$. (g) Cycle stability at 10 A g^{-1}.

structural stability.

The reaction kinetics was investigated. Fig. 5a shows the superior electrochemical properties of $MoSe_2$/MCFs@NC at scan rates of 0.2 to 1.0 mV s^{-1}. All redox peaks are almost identical, suggesting a distinct pseudocapacitive behavior, and also indicating fast kinetics and low electrode polarization. Generally, the captured redox peak current (i) and scan rate (v) conform to the equation: $\log i = b\log v + \log a$, where b is originated from the slope of the $\log i$ *vs.* $\log v$ curve as an indicator for judging the type of charge storage mechanism. The value of b approaching 0.5 indicates that the diffusion-dominated reaction process and near 1 shows a capacitive effect. Available from Fig. 5a, the b-values of the $MoSe_2$/MCFs@NC electrode are calculated from the linear fit of the five labeled peaks of the CV curves presented in Fig. 5b. The b-values of 0.91, 0.95, 0.89, 0.98, and 0.88 are calculated according to the peaks 1, 2, 3, 4, and 5, respectively, showing that its electrochemical process mainly depends on the surface-induced capacitive process. The relative pseudocapacitive contribution could be determined from the following equation: $i = k_1v + k_2v^{0.5}$, where k_1v represents the pseudocapacitive behavior, and $k_2v^{0.5}$ suggests the diffusion behavior. Fig. 5c demonstrates 92.3% contribution of pseudocapacitance. At scan speeds of 0.2, 0.4, 0.6, 0.8, and 1.0 mV s^{-1}, the pseudocapacitive contributions can reach 90.1%, 90.5%, 91.3%, 91.9%, and 92.3%, respectively (Fig. 5d and Fig. S8). Fig. 5e shows the galvanostatic intermittent titration technique curves of the $MoSe_2$/MCFs@NC electrodes between 0.01 and 3.0 V. The overpotential at the appropriate sodiation/desodiation stage is represented by the potential change for each relaxation cycle. After calculations, the plots of the D_{Na^+} values of $MoSe_2$/MCFs@NC are shown in Fig. 5f, showing a good kinetics process. EIS is also measured and shown in Fig. S9. From the circuit diagram, CPE_1 is the constant phase element, and W_1 is the Warburg impedance. R_1 and R_2 are the ohmic resistance and charge transfer resistance. Compared with the EIS of $MoSe_2$/MCFs and $MoSe_2$, the R_2 value of the $MoSe_2$/MCFs@NC electrode is only 15 Ω, which is much lower than that of the $MoSe_2$/MCFs and $MoSe_2$ electrodes, indicating much faster charge transport kinetics for $MoSe_2$/MCFs@NC.

Considering the attractive sodium storage property of $MoSe_2$/MCFs@NC, the $MoSe_2$/MCFs@NC anode was assembled into a sodium-ion full cell by blending with the $Na_3V_2(PO_4)_2O_2F$

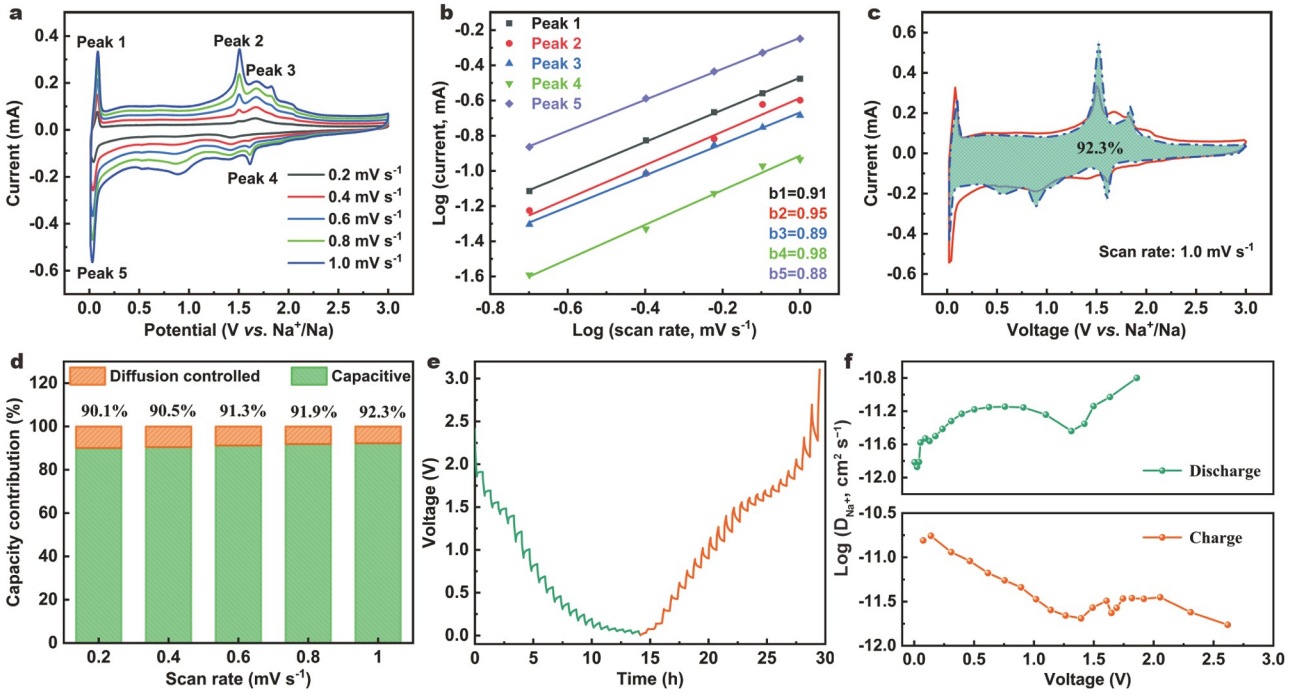

Figure 5 Kinetics analyses of the $MoSe_2$/MCFs@NC electrode. (a) CV curves. (b) The corresponding log*i* *versus* log*v* plots. (c) Capacitive contribution at 1.0 mV s^{-1}. (d) The contribution ratios of the pseudocapacitive part at different scan rates. (e) Galvanostatic intermittent titration technique curves and (f) the calculated sodium-ion diffusion coefficients.

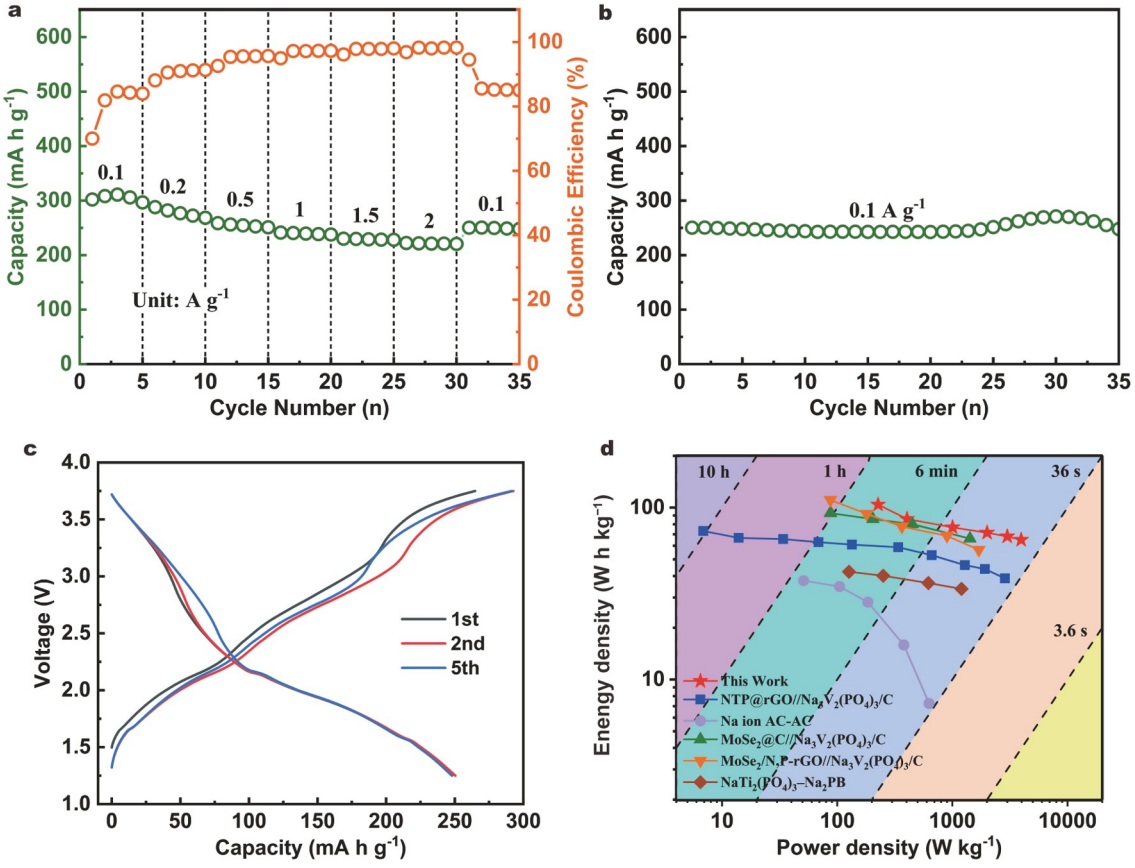

Figure 6 Electrochemical performance of the $MoSe_2$/MCFs@NC//NVPOF full cell. (a) Rate performance from 0.1 to 2 A g^{-1}. (b) Cycle stability at 0.1 A g^{-1}. (c) Galvanostatic discharge-charge curves. (d) Comparison of Ragone plots of the $MoSe_2$/MCFs@NC//NVPOF full cell with other sodium-ion full cells.

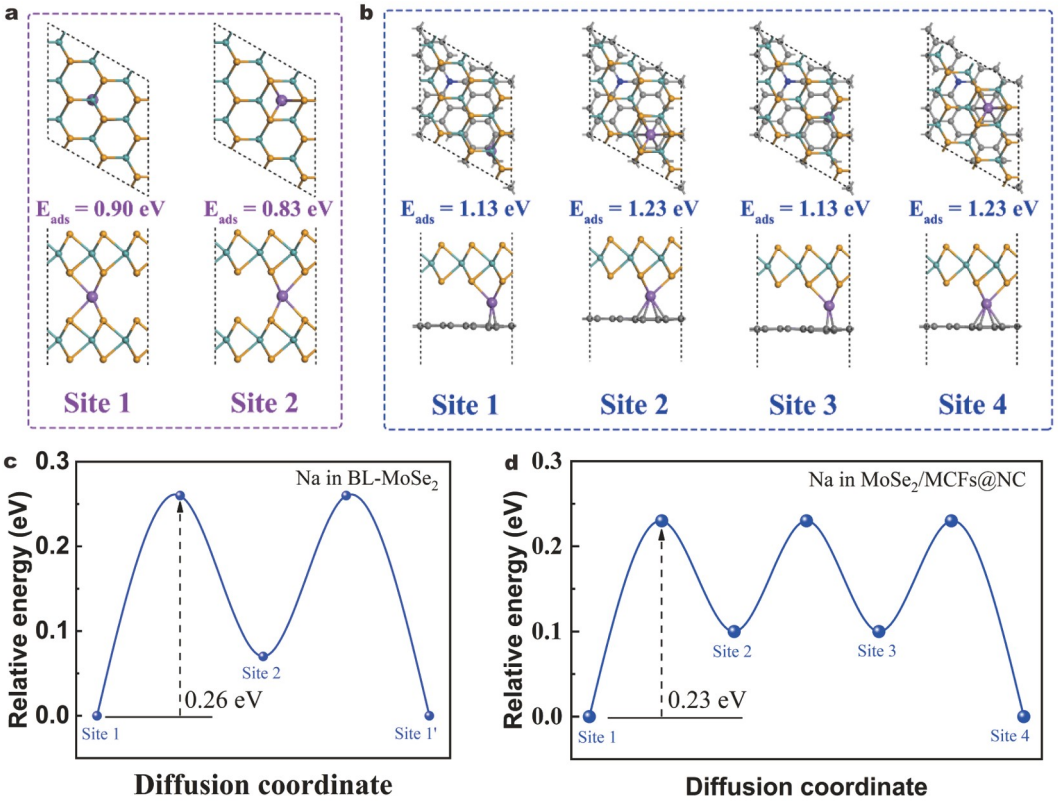

Figure 7 The optimized structures (both top views and side views) of (a) Na adsorbed BL-$MoSe_2$ and (b) Na adsorbed $MoSe_2$/MCFs@NC. Different adsorption sites and the corresponding E_{ads} values are provided. The purple, orange, cyan, blue, and gray spheres denote Na, Se, Mo, N, and C atoms, respectively. The diffusion pathway and the energy profile of Na on (c) the interlayer of BL-$MoSe_2$ and (d) the interlayer of $MoSe_2$/MCFs@NC. All the energies are relative to the lowest-energy configuration.

(NVPOF) cathode. Fig. 6a and Fig. S10 illustrate the capacities of 311, 276, 254, 239, 229, and 221 mA h g^{-1} can be recorded at 0.1, 0.2, 0.5, 1, 1.5, and 2 A g^{-1}. In the subsequent cycles (Fig. 6b), the discharge capacity of the full cell can achieve 250 mA h g^{-1} (GCD curves in Fig. 6c) at 0.1 A g^{-1} over 35 cycles. Furthermore, the light-emitting diodes (LEDs) are successfully lighted by the $MoSe_2$/MCFs@NC//NVPOF full cell (inset Fig. 6b), demonstrating the practical application. The Ragone plot (Fig. 6d) exhibits the $MoSe_2$/MCFs@NC//NVPOF and other sodium-ion full cells [26,47,53–55]. At a power density of 226 W kg^{-1}, the assembled full cell delivers 104 W h kg^{-1} of energy. More impressively, it keeps 65 W h kg^{-1} at a higher power density of 3960 W kg^{-1}, which presents the promising practical applications of the obtained $MoSe_2$/MCFs@NC electrode.

Storage mechanisms of Na^+ in BL-$MoSe_2$, $MoSe_2$/MCFs, and $MoSe_2$/MCFs@NC were detailed compared by DFT calculations. In the interlayer of BL-$MoSe_2$, two stable adsorption sites for Na can be seen: the top site on the Mo atom (Site 1) and the hollow site (Site 2); corresponding E_{ads} are 0.90 and 0.83 eV, respectively, as illustrated in Fig. 7a. For the interface of the $MoSe_2$/MCFs@NC heterostructure (Fig. 7b), the adsorption energies of Na are 1.13 eV on Site 1 and Site 3 (top site on Mo and C atom), as well as 1.23 eV on Site 2 and Site 4 (both hollow sites on $MoSe_2$ and MCFs). Thus, the adsorption of Na^+ in the interface of $MoSe_2$/MCFs@NC will be stronger than that in the interlayer of BL-$MoSe_2$. The diffusion barriers of Na ions in the interlayer of BL-$MoSe_2$ and $MoSe_2$/MCFs@NC were also checked. Fig. 7c, d depict the energy map for Na ion diffusion. As can be calculated, the diffusion barrier of Na in the interlayer of $MoSe_2$/MCFs@NC (0.23 eV) is lower than that in the interlayer of BL-$MoSe_2$ (0.26 eV). Therefore, the computational results confirm that the formation of $MoSe_2$/MCFs@NC heterostructure not only enables enhanced binding of Na ions in the interlayer, but also leads to faster diffusion of Na ions.

CONCLUSIONS

In summary, electronic modulation and structural engineering were used to design a N-doped dual carbon-coated $MoSe_2$ with multichannel paths ($MoSe_2$/MCFs@NC). Owing to sufficient ion/electron transport channels, excellent electrical conductivity, and abundant exposed active sites, $MoSe_2$/MCFs@NC exhibits superior electrochemical properties in SIBs. When served as the anode of the SIB half-cell, the $MoSe_2$/MCFs@NC exhibits a capacity of 411 mA h g^{-1} at 0.2 A g^{-1} with an outstanding stability of the appreciable capacity of 303 mA h g^{-1} after 1100 cycles at 10 A g^{-1}. The computational calculation was performed to further prove the improved SIBs performance of the $MoSe_2$/MCFs@NC heterostructure, which can enable enhanced binding of Na ions in the interlayer and accelerate the diffusion of Na ions simultaneously. The full SIBs performance shows the construction of transition metal selenides with multichannel paths favors their potential application in energy storage devices.

Received 1 March 2022; accepted 22 April 2022; published online 8 July 2022

1 Luo L, Zhou K, Lian R, *et al.* Cation-deficient TiO_2(B) nanowires with protons charge compensation for regulating reversible magnesium storage. Nano Energy, 2020, 72: 104716

2 Wang B, Cheng Y, Su H, *et al.* Boosting transport kinetics of cobalt sulfides yolk-shell spheres by anion doping for advanced lithium and sodium storage. ChemSusChem, 2020, 13: 4078–4085
3 Cheng C, Zang X, Hou W, *et al.* Construction of three-dimensional electronic interconnected $Na_3V_2(PO_4)_3$/C as cathode for sodium ion batteries. J Alloys Compd, 2022, 899: 163363
4 Zuo W, Liu X, Qiu J, *et al.* Engineering Na^+-layer spacings to stabilize Mn-based layered cathodes for sodium-ion batteries. Nat Commun, 2021, 12: 4903
5 Jiang LL, Yan C, Yao YX, *et al.* Inhibiting solvent Co-intercalation in a graphite anode by a localized high-concentration electrolyte in fast-charging batteries. Angew Chem Int Ed, 2021, 60: 3402–3406
6 Hou J, Hadouchi M, Sui L, *et al.* Unlocking fast and reversible sodium intercalation in NASICON $Na_4MnV(PO_4)_3$ by fluorine substitution. Energy Storage Mater, 2021, 42: 307–316
7 Zhang L, Li X, Tai L, *et al.* Constructing electronic interconnected bimetallic selenide-filled porous carbon nanosheets for stable and highly efficient sodium-ion half/full batteries. Nanoscale, 2021, 13: 18578–18585
8 Su G, Chen S, Dong H, *et al.* Tuning the electronic structure of layered vanadium pentoxide by pre-intercalation of potassium ions for superior room/low-temperature aqueous zinc-ion batteries. Nanoscale, 2021, 13: 2399–2407
9 Hu Y, Yu Q, Tang W, *et al.* Ultra-stable, ultra-long-lifespan and ultra-high-rate Na-ion batteries using small-molecule organic cathodes. Energy Storage Mater, 2021, 41: 738–747
10 Xiao S, Li X, Zhang W, *et al.* Bilateral interfaces in In_2Se_3-$CoIn_2$-$CoSe_2$ heterostructures for high-rate reversible sodium storage. ACS Nano, 2021, 15: 13307–13318
11 Yang M, Sun Z, Nie P, *et al.* $SbPS_4$: A novel anode for high-performance sodium-ion batteries. Chin Chem Lett, 2022, 33: 470–474
12 Li Q, Yang D, Chen H, *et al.* Advances in metal phosphides for sodium-ion batteries. SusMat, 2021, 1: 359–392
13 Zhou S, Liu S, Chen W, *et al.* A "biconcave-alleviated" strategy to construct *aspergillus niger*-derived carbon/MoS_2 for ultrastable sodium ion storage. ACS Nano, 2021, 15: 13814–13825
14 Li P, Guo X, Zang R, *et al.* Nanoconfined SnO_2/$SnSe_2$ heterostructures in N-doped carbon nanotubes for high-performance sodium-ion batteries. Chem Eng J, 2021, 418: 129501
15 Liu C, Zhang M, Zhang X, *et al.* 2D sandwiched nano heterostructures endow $MoSe_2$/TiO_{2-x}/graphene with high rate and durability for sodium ion capacitor and its solid electrolyte interphase dependent sodiation/desodiation mechanism. Small, 2020, 16: 2004457
16 Ge JM, Fan L, Wang J, *et al.* $MoSe_2$/N-doped carbon as anodes for potassium-ion batteries. Adv Energy Mater, 2018, 8: 1801477
17 Choi W, Choudhary N, Han GH, *et al.* Recent development of two-dimensional transition metal dichalcogenides and their applications. Mater Today, 2017, 20: 116–130
18 Sun Z, Wu XL, Xu J, *et al.* Construction of bimetallic selenides encapsulated in nitrogen/sulfur co-doped hollow carbon nanospheres for high-performance sodium/potassium-ion half/full batteries. Small, 2020, 16: 1907670
19 Yang J, Hou W, Pan R, *et al.* The interfacial electronic engineering in polyhedral MOF derived Co-doped $NiSe_2$ composite for upgrading rate and longevity performance of aqueous energy storage. J Alloys Compd, 2022, 897: 163187
20 Yousaf M, Wang Y, Chen Y, *et al.* A 3D trilayered CNT/$MoSe_2$/C heterostructure with an expanded $MoSe_2$ interlayer spacing for an efficient sodium storage. Adv Energy Mater, 2019, 9: 1900567
21 Su Q, Cao X, Yu T, *et al.* Binding $MoSe_2$ with dual protection carbon for high-performance sodium storage. J Mater Chem A, 2019, 7: 22871–22878
22 Yi Y, Sun Z, Li C, *et al.* Designing 3D biomorphic nitrogen-doped $MoSe_2$/graphene composites toward high-performance potassium-ion capacitors. Adv Funct Mater, 2020, 30: 1903878
23 Huang Y, Wang Z, Guan M, *et al.* Toward rapid-charging sodium-ion batteries using hybrid-phase molybdenum sulfide selenide-based anodes. Adv Mater, 2020, 32: 2003534
24 Liu H, Guo H, Liu B, *et al.* Few-layer $MoSe_2$ nanosheets with expanded (002) planes confined in hollow carbon nanospheres for ultrahigh-performance Na-ion batteries. Adv Funct Mater, 2018, 28: 1707480
25 Wu J, Yu J, Liu J, *et al.* $MoSe_2$ nanosheets embedded in nitrogen/phosphorus co-doped carbon/graphene composite anodes for ultrafast sodium storage. J Power Sources, 2020, 476: 228660
26 Liu Y, Wang N, Zhao X, *et al.* Hierarchical nanoarchitectured hybrid electrodes based on ultrathin $MoSe_2$ nanosheets on 3D ordered macroporous carbon frameworks for high-performance sodium-ion batteries. J Mater Chem A, 2020, 8: 2843–2850
27 Li T, Zhang H, Tang Y, *et al.* Hybrid-cyanogels induced sandwich-like N,P-carbon/$SnNi_{10}P_3$ for excellent lithium storage. ACS Appl Energy Mater, 2019, 2: 3683–3691
28 Yang J, Yang N, Xu Q, *et al.* Bioinspired controlled synthesis of NiSe/Ni_2P nanoparticles decorated 3D porous carbon for Li/Na ion batteries. ACS Sustain Chem Eng, 2019, 7: 13217–13225
29 Li T, Wang A, Li X, *et al.* $MoS_{0.5}Se_{1.5}$ embedded in 2D porous carbon sheets boost lithium storage performance as an anode material. Adv Mater Interfaces, 2018, 5: 1701604
30 Perdew JP, Burke K, Ernzerhof M. Generalized gradient approximation made simple. Phys Rev Lett, 1996, 77: 3865–3868
31 Grimme S. Semiempirical GGA-type density functional constructed with a long-range dispersion correction. J Comput Chem, 2006, 27: 1787–1799
32 Govind N, Petersen M, Fitzgerald G, *et al.* A generalized synchronous transit method for transition state location. Comput Mater Sci, 2003, 28: 250–258
33 Li W, Bi R, Liu G, *et al.* 3D interconnected MoS_2 with enlarged interlayer spacing grown on carbon nanofibers as a flexible anode toward superior sodium-ion batteries. ACS Appl Mater Interfaces, 2018, 10: 26982–26989
34 Zhou F, Xin S, Liang HW, *et al.* Carbon nanofibers decorated with molybdenum disulfide nanosheets: Synergistic lithium storage and enhanced electrochemical performance. Angew Chem Int Ed, 2014, 53: 11552–11556
35 Ni X, Cui Z, Luo H, *et al.* Hollow multi-nanochannel carbon nanofibers@$MoSe_2$ nanosheets composite as flexible anodes for high performance lithium-ion batteries. Chem Eng J, 2021, 404: 126249
36 Xie X, Huang K, Wu X, *et al.* Binding hierarchical $MoSe_2$ on MOF-derived N-doped carbon dodecahedron for fast and durable sodium-ion storage. Carbon, 2020, 169: 1–8
37 Zhao X, Cai W, Yang Y, *et al.* $MoSe_2$ nanosheets perpendicularly grown on graphene with Mo–C bonding for sodium-ion capacitors. Nano Energy, 2018, 47: 224–234
38 Liang Q, Zhang L, Zhang M, *et al.* Three-dimensional hierarchical $MoSe_2$/N,F co-doped carbon heterostructure assembled by ultrathin nanosheets for advanced lithium-ion batteries. ACS Sustain Chem Eng, 2020, 8: 14127–14136
39 Damien D, Anil A, Chatterjee D, *et al.* Direct deposition of $MoSe_2$ nanocrystals onto conducting substrates: Towards ultra-efficient electrocatalysts for hydrogen evolution. J Mater Chem A, 2017, 5: 13364–13372
40 Park GD, Kim JH, Park SK, *et al.* $MoSe_2$ embedded CNT-reduced graphene oxide composite microsphere with superior sodium ion storage and electrocatalytic hydrogen evolution performances. ACS Appl Mater Interfaces, 2017, 9: 10673–10683
41 Chen J, Pan A, Wang Y, *et al.* Hierarchical mesoporous $MoSe_2$@CoSe/N-doped carbon nanocomposite for sodium ion batteries and hydrogen evolution reaction applications. Energy Storage Mater, 2019, 21: 97–106
42 Kim JK, Lim KE, Hwang WJ, *et al.* Hierarchical tubular-structured $MoSe_2$ nanosheets/N-doped carbon nanocomposite with enhanced sodium storage properties. ChemSusChem, 2020, 13: 1546–1555
43 Wang Q, Ge X, Xu J, *et al.* Fabrication of microporous sulfur-doped carbon microtubes for high-performance sodium-ion batteries. ACS Appl Energy Mater, 2018, 1: 6638–6645
44 Hou BH, Wang YY, Ning QL, *et al.* Self-supporting, flexible, additive-free, and scalable hard carbon paper self-interwoven by 1D microbelts: Superb room/low-temperature sodium storage and working mechanism. Adv Mater, 2019, 31: 1903125
45 Hou H, Banks CE, Jing M, *et al.* Carbon quantum dots and their

derivative 3D porous carbon frameworks for sodium-ion batteries with ultralong cycle life. Adv Mater, 2015, 27: 7861–7866
46 Zhang L, Dong H, Wei H, *et al.* Interface and structure engineering of bimetallic selenides toward high-performance sodium-ion half/full batteries. J Power Sources, 2021, 506: 230216
47 Niu F, Yang J, Wang N, *et al.* $MoSe_2$-covered N, P-doped carbon nanosheets as a long-life and high-rate anode material for sodium-ion batteries. Adv Funct Mater, 2017, 27: 1700522
48 Zhang Y, Liu Z, Zhao H, *et al.* $MoSe_2$ nanosheets grown on carbon cloth with superior electrochemical performance as flexible electrode for sodium ion batteries. RSC Adv, 2016, 6: 1440–1444
49 Li Y, Han M, Zhou Z, *et al.* Topological insulator-assisted $MoSe_2/Bi_2Se_3$ heterostructure: Achieving fast reaction kinetics toward high rate sodium-ion batteries. ChemElectroChem, 2021, 8: 697–704
50 Li J, Hu H, Qin F, *et al.* Flower-like $MoSe_2$/C composite with expanded (002) planes of few-layer $MoSe_2$ as the anode for high-performance sodium-ion batteries. Chem Eur J, 2017, 23: 14004–14010
51 Zhang Y, Deng S, Shen Y, *et al.* Construction of 1T-$MoSe_2$/TiC@C branch-core arrays as advanced anodes for enhanced sodium ion storage. ChemSusChem, 2020, 13: 1575–1581
52 Qin F, Hu H, Jiang Y, *et al.* Mesoporous $MoSe_2$/C composite as anode material for sodium/lithium ion batteries. J Electroanal Chem, 2018, 823: 67–72
53 Chen Z, Augustyn V, Jia X, *et al.* High-performance sodium-ion pseudocapacitors based on hierarchically porous nanowire composites. ACS Nano, 2012, 6: 4319–4327
54 Fang Y, Xiao L, Qian J, *et al.* 3D graphene decorated $NaTi_2(PO_4)_3$ microspheres as a superior high-rate and ultracycle-stable anode material for sodium ion batteries. Adv Energy Mater, 2016, 6: 1502197
55 Wu X, Cao Y, Ai X, *et al.* A low-cost and environmentally benign aqueous rechargeable sodium-ion battery based on $NaTi_2(PO_4)_3$-$Na_2NiFe(CN)_6$ intercalation chemistry. Electrochem Commun, 2013, 31: 145–148

Acknowledgements This work was financially supported by the National Natural Science Foundation of China (51801030), the Natural Science Foundation of Guangdong Providence (2018A030310571), the Science and Technology Development Plan of Suzhou (ZXL2021176), China Postdoctoral Science Foundation (2022M711686) and Jiangsu Provincial Funds for the Young Scholars (BK20190978). The authors acknowledge Prof. Youyong Li from Soochow University for the support of the computational tool.

Author contributions Lv C and Lin C performed the experiment, analyzed the data, and wrote the original draft. Dong H conducted the DFT calculation. Wei H participated in the investigation and revised the paper. Yang J and Geng H conducted the conceptualization and revised the paper. All authors contributed to the general discussion.

Conflict of interest The authors declare that they have no conflict of interest.

Supplementary information Supporting data are available in the online version of the paper.

Jun Yang received his PhD degree from Nanjing Tech University (China) in 2018. He is now working as a lecturer at Jiangsu University of Science and Technology. His research interest focuses on functional materials for energy-related applications.

Hongbo Geng received his PhD degree from Soochow University (China) in 2017. He is now working as a full professor at Changshu Institute of Technology. His current research interests focus on functional nanomaterials for electrochemical storage.

电子调制和结构设计具有多通道传输的二硒化钼应用于高性能钠离子电池

吕成魁[1,2†], 蔺春发[2†], 董慧龙[2†], 魏怀鑫[1*], 杨骏[3*], 耿洪波[2*]

摘要 由于钠资源储量丰富且价格低廉，钠离子电池(SIBs)可作为锂离子电池(LIBs)的有效替代品已成为共识. 基于此，开发适合钠存储的电极材料是钠离子电池发展的关键. 近年来，二维层状过渡金属硫属化物在能源和环境领域受到广泛关注. 其中$MoSe_2$，由于其宽的层间距和较高电导率，被认为是一种具有潜力的SIBs负极材料. 本工作中，我们通过静电纺丝，硒化及碳化过程，设计制造了具有多通道电子传输路径的氮掺杂双碳壳层$MoSe_2$纳米材料($MoSe_2$/MCFs@NC). 此结构具有三维连通的导电网络，丰富的空隙和足够的电子传输路径，有助于适应钠离子脱嵌带来的体积膨胀应力，并加快电荷转移动力学. 作为钠离子电池负极材料时，$MoSe_2$/MCFs@NC表现出高的比容量(10 A g^{-1}电流密度下为319 mA h g^{-1})和优异的循环稳定性(10 A g^{-1}的电流密度下可循环1100圈). 此外，该材料在与$Na_3V_2(PO_4)_2O_2F$正极材料组成的钠离子全电池中也表现出了卓越的性能. 理论计算进一步验证了双碳壳层和$MoSe_2$之间的强相互作用，对于提升$MoSe_2$/MCFs@NC的钠离子电池综合性能具有重要意义. 本研究为制备高性能钠离子电池电极材料提供了新思路.

